Research Article | Vol. 14, No. 3 / 1 Mar 2024 / Optical Materials Express 778
Optical Materials EXPRESS

Broadband Ag/SiO_2/Fe/TiO_2 ultrathin planar absorber with a wide acceptance angle from visible to near-infrared regions

YUUSUKE TAKASHIMA,[1,2,*] SHUNSUKE FURUTA,[3] KENTARO NAGAMATSU,[1,2] MASANOBU HARAGUCHI,[1,2] AND YOSHIKI NAOI[1,2]

[1]*Graduate School of Technology, Industrial and Social Science, Tokushima University, Tokushima 770-8506, Japan*
[2]*Institute of Post-LED Photonics, Tokushima University 770-8506, Japan*
[3]*Graduate School of Sciences and technology for innovation, Tokushima University 770-8506, Japan*
[*]*takashima@tokushima-u.ac.jp*

Abstract: We present theoretical and experimental evidences of a broadband ultrathin optical absorber, constructed using Ag(85 nm)/SiO_2(70 nm)/Fe(13 nm)/TiO_2(60 nm) planar films, with a wide acceptance angle and effective admittance similar to that of air. Calculations show that this system displays near-complete visible to near-infrared absorption owing to admittance matching. The electromagnetic distribution within the layered film reveals that the high absorption rate is primarily attributed to the deep subwavelength Fe film. Maximum absorption of 99.3% is achieved even with a 13-nm-thick Fe absorptive film, and an average absorption rate of 94.8% is observed in the 400–1100 nm wavelength range. Notably, even at 60° oblique incidence, the fabricated absorber sustains an absorption rate of 85.4% (for unpolarized light). Such absorbers can be applied to efficient thermal generation and various other applications owing to their minimal heat capacity, expansive area, and fabrication simplicity.

1. Introduction

The fundamental physical property of light absorption has been extensively studied for various applications, including solar cell [1,2], photodetectors [3,4], thermophotovoltaics [5,6], and thermal emitters [7,8]. Such devices are adept at converting light into voltage, photocurrent, or heat. For these technologies, a broadband-perfect light absorber that demonstrates substantial angular tolerance is crucial for effective conversion. Notably, an absorber that is considerably thinner than the incident wavelength (λ) can significantly amplify the efficiency of light–heat or light–photocurrent conversions due to its reduced heat capacity and thickness smaller than the carrier's diffusion length [4].

Achieving perfect absorption (A) necessitates the suppression of both reflection (R) and transmission (T). The concurrent suppression of T and R poses challenges, given that absorptive materials typically exhibit highly reflective surfaces. To augment optical absorption, recent research has intensely explored light manipulation via subwavelength-scale resonators such as plasmonic structures and metamaterials [9–20]. The optical characteristics of nanoscale resonators, including R and T, can be deliberately modified by adjusting their geometries. An aptly designed resonator can trap light within the subwavelength region, thereby magnifying optical absorption. Although advanced and precise nanofabrication methods, such as electron beam lithography and focused ion beam sputtering, are requisite, subwavelength resonators have both theoretically and empirically shown near-perfect absorption spanning from the visible (VIS) to microwave spectrum.

Another viable and cost-efficient method to attain perfect absorption involves utilizing planar films on reflective metal substrates. The Dällenbach and Salisbury absorbers serve as paradigmatic

#517239 https://doi.org/10.1364/OME.517239
Journal © 2024 Received 28 Dec 2023; revised 10 Feb 2024; accepted 12 Feb 2024; published 26 Feb 2024

Optical Materials EXPRESS

examples of film absorbers [21,22]. Their functioning relies on the destructive interference of reflection by a $\lambda/4$ film placed on a perfect electric conductor substrate. Utilizing this principle of destructive interference, multiple research groups have unveiled exemplary planar absorbers [21–25]. Importantly, the stacked film system offers considerable advantages in terms of fabrication as it circumvents the need for expensive or intricate nanofabrication procedures.

Recent studies demonstrated that ultrathin highly lossy films (whose refractive indices' real (n) and imaginary (k) parts are of the same order), such as Si, Ge, TiO_2, Cr, Fe, VO_2, and $Ge_2Sb_2Te_5$ (GST) placed on reflective substrates exhibit substantial broadband absorption from the deep ultraviolet to the infrared regions [26–42]. The phase change in the highly lossy films is nontrivial (not 0 or π) owing to their high complex refractive indices, and the Fresnel coefficients at each interface of these lossy films are distant from the real axis within the complex plane. Because of these features, both T and R are cancelled even when the thickness of the lossy film is significantly thinner than λ because thickness-induced phase control is not essential for obtaining destructive interference. Several research groups have successfully fabricated perfect ultra-broadband absorbers using light absorption facilitated by multi-absorptive semiconductor or metal layers [30,33,34,38]. From perspective of the light–heat or light–photocurrent conversions, broadband perfect light absorption within a singular ultrathin absorptive film is conducive to amplifying both photoelectric and photothermal conversion efficiencies. However, realizing broadband absorption into a single ultrathin absorptive film is challenging because chromatic dispersion of the refractive index of each film disturbs the interference condition.

In this study, we demonstrated near-perfect ultra-broadband absorption in a single nanoscale-thin film by embedding a single ultrathin Fe film between high-refractive-index (high-n: TiO_2) and low-refractive-index (low-n: SiO_2) transparent dielectric films on a reflective Ag substrate. The novel combination of Ag, SiO_2, Fe, and TiO_2 maintains the destructive interference condition at broadband wavelengths owing to complementary indices of these individual component materials. Our strategically designed planar absorber provides a comprehensive suppression of both R and T, facilitating near-perfect absorption for an ultrathin, highly lossy single Fe film in the VIS to near-infrared (NIR) range. The optical admittance diagram of our assembly underscores the synergy between the high-n and low-n transparent films. This synergy is pivotal in achieving admittance matching and in sustaining the T and R cancellation across an expansive wavelength range. Our fabricated absorber experimentally recorded an average absorption rate of 94.8% spanning from VIS to NIR wavelengths, with a peak absorption rate of 99.3%. Simulations using the finite-difference time-domain (FDTD) method reveal that almost all incident light is absorbed by the singular, much thinner, highly lossy film layer compared to the λ. Additionally, our absorber demonstrated a reduced dependency on the incident angle, preserving its high absorption capacity even at an oblique incidence of 60°.

2. Design of broadband nano-order perfect absorber

Figure 1 depicts an analytical model of the proposed planar absorber. This model consists of five layers: a reflective metal substrate, a transparent film with a low-refractive-index (low-n), a highly lossy film, a transparent film with a high-refractive-index (high-n), and the incident medium. The incident medium is assumed to be air, and both the substrate and incident medium have infinite thicknesses. The thicknesses of the transparent low-n, highly lossy, and transparent high-n films are represented as t_{low-n}, t_{lossy}, and t_{high-n}, respectively. The symbol θ denotes the angle of incidence. To achieve perfect absorption, both T and R must be simultaneously nullified. In our design, an infinitely thick reflective metal substrate serves as an almost perfect reflector, preventing light from being transmitted (reducing T to nearly zero). Light partially reflected at the surface of each film interferes with the incident beam. This destructive interference between the reflected waves minimizes R and effectively confines the incident light within the layered structure. Hence, the highly lossy film captures and absorbs the incident light completely. The

Optical Materials EXPRESS

considerably complex refractive index values of this absorptive film cause its Fresnel coefficients to deviate substantially from the real axis in the complex plane, and this causes a nontrivial (not 0 or π) phase shift in the reflected waves [26,27,31]. Such conditions facilitate extraordinarily destructive interference, enabling near-perfect absorption in an absorptive layer considerably thinner than the wavelength. In particular, the combination of transparent films with low and high refractive indices is vital for sustaining these destructive interference conditions across a wide range of wavelengths. Introducing a transparent low-n film between the reflective substrate and the highly absorptive layer modulates the refractive index contrast over a broad wavelength spectrum, particularly as typical reflective materials, such as metals, possess nearly zero n and high k values. Additionally, the transparent high-n film compensates for the amplitude and phase shifts of the Fresnel coefficients at the interface involving the reflective substrate, low-n film, highly absorptive film, and air. This distinctive asymmetrical refractive index configuration flanking the absorptive layer ensures a broadband optical admittance match between the stacked films and the surrounding air. Hence, exceptionally thin lossy films can achieve perfect ultra-broadband absorption.

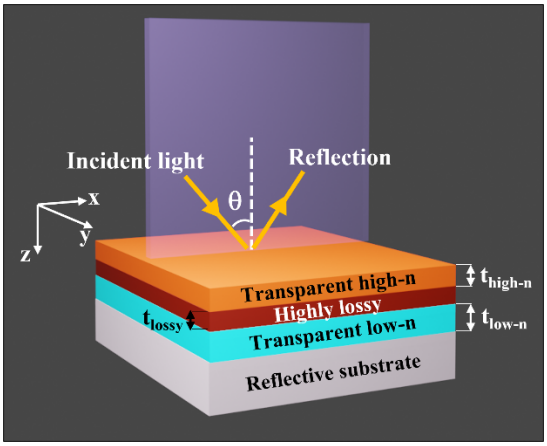

Fig. 1. Schematic of our proposed absorber.

To verify our design concept, we analyzed the normal reflection spectra using the transfer matrix method (TMM). We selected Ag for the metal substrate because of its nearly perfect light reflection capability across VIS to NIR wavelengths (For example, refractive index of Ag: $0.0500 + 2.1035i$ at $\lambda = 400$ nm, $0.0410 + 4.8025i$ at $\lambda = 700$ nm, and $0.0400 + 7.1155i$ at $\lambda = 1000$ nm) [43].

The Fe was chosen as the highly absorptive film given that both the real and imaginary components of its refractive index are comparable and high over the extensive wavelength range from VIS to NIR (The refractive index of Fe: $2.2606 + 2.5931i$ at $\lambda = 400$ nm, $2.8653 + 3.1820i$ at $\lambda = 700$ nm, and $2.9277 + 3.8315i$ at $\lambda = 1000$ nm) [44]. The refractive index of Fe shows small chromatic dispersion, especially its real part. This is attractive for realizing broadband absorption because the interference condition can be maintained in broadband wavelength. Moreover, Fe possesses advantages for the practical use of the optical absorber owing to its very low cost.

We incorporated SiO_2 and TiO_2 as transparent low-n and high-n films, respectively, due to their appropriate refractive indices and pronounced transparency within this spectral range (The refractive index of SiO_2: 1.4897 at $\lambda = 400$ nm, 1.4745 at $\lambda = 700$ nm, and 1.4707 at $\lambda = 1000$ nm, TiO_2: 2.3379 at $\lambda = 400$ nm, 2.1126 at $\lambda = 700$ nm, and 2.0757 at $\lambda = 1000$ nm) [45,46].

We investigated the dependence of the reflectivity on the Fe film thickness. Figure 2 (a)-(l) show the dependence of the reflectivity on the thickness of Fe (t_{lossy}), TiO_2, and SiO_2 at the

Optical Materials EXPRESS

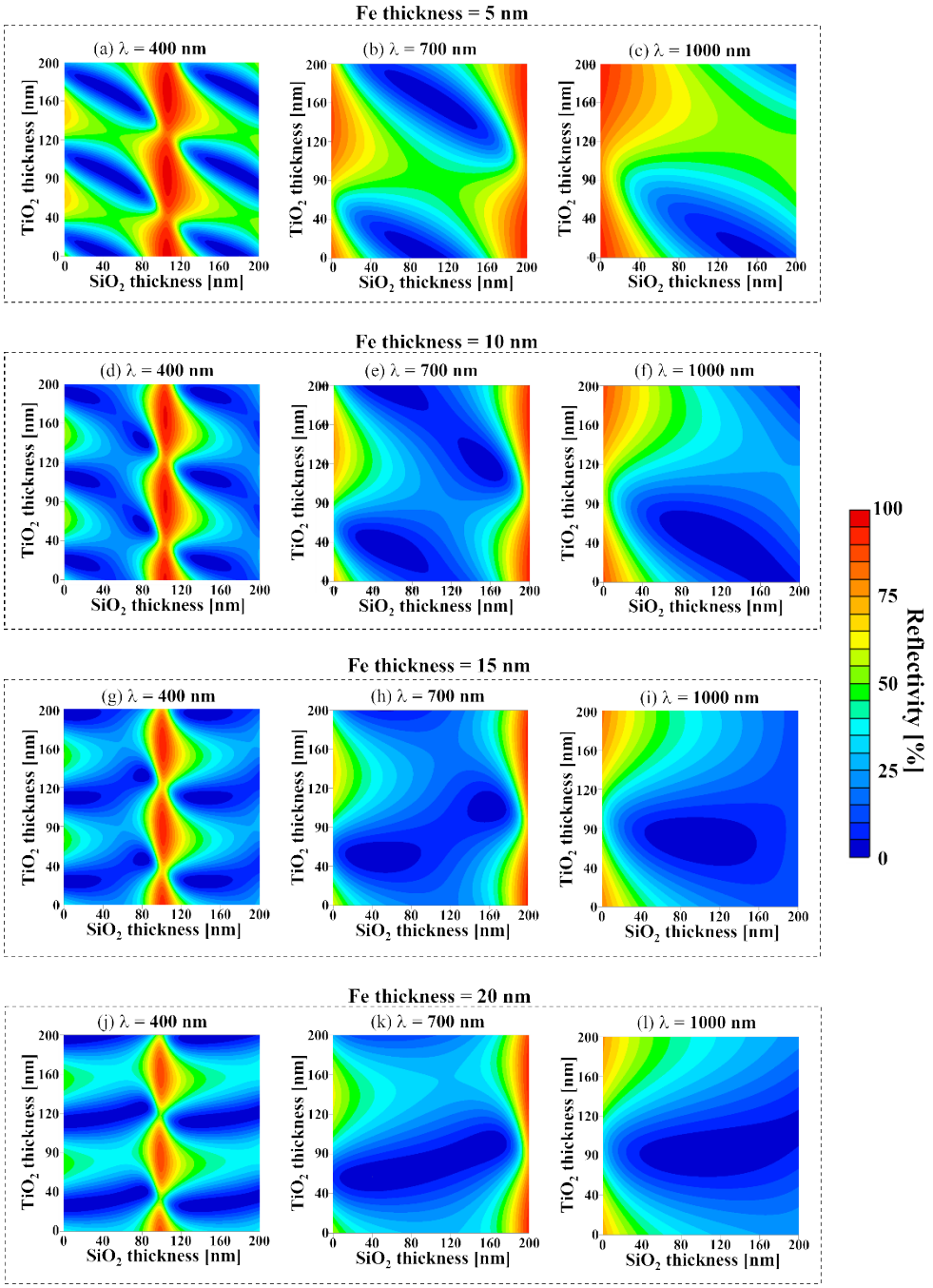

Fig. 2. Calculated reflectivity contours for various thicknesses of Fe, SiO_2, and TiO_2.

typical wavelengths. For the $t_{lossy} = 5$ nm, the low reflection region (depicted as deep blue in Fig. 2) is obviously out of position at each wavelength. With increasing the thickness of Fe from 5 nm to 15 nm, the low reflection region at each wavelength tends to overlap. However, the position mismatch of the low reflection region increases at the shorter wavelength when

Optical Materials EXPRESS

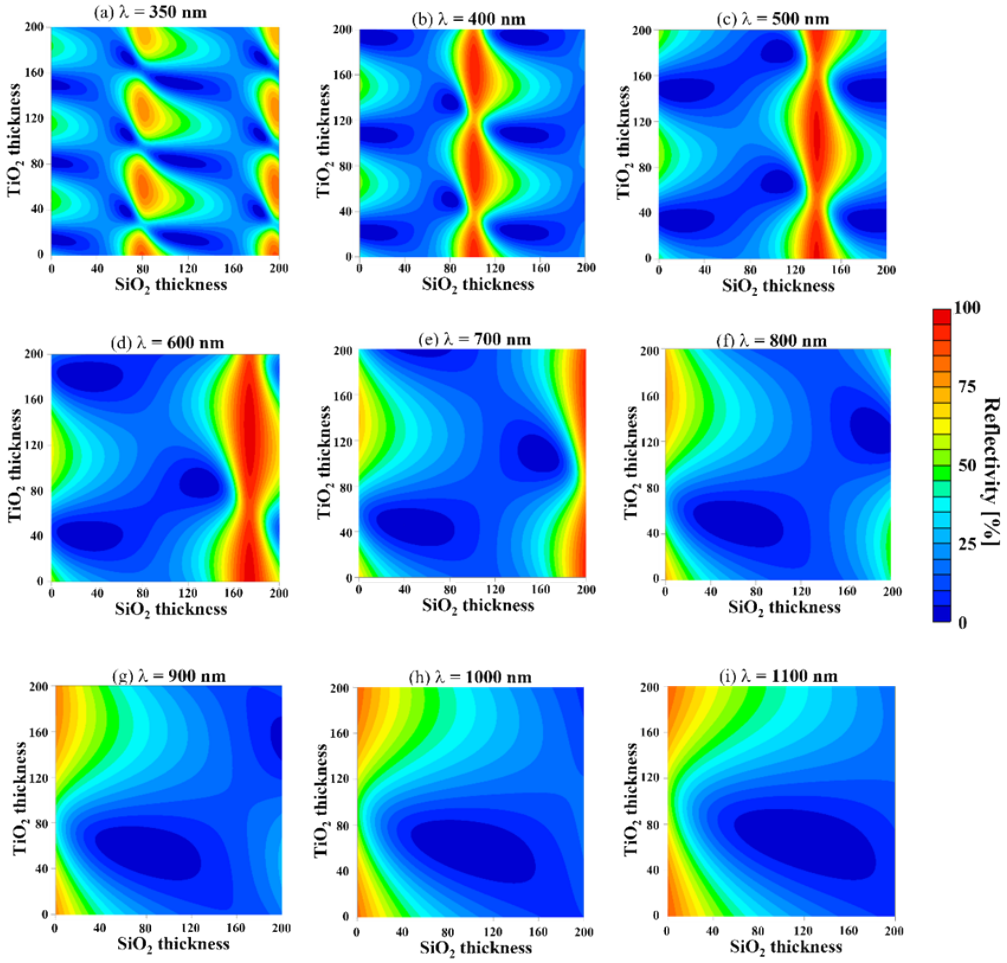

Fig. 3. Calculated dependence of the reflectivity on both thickness of SiO_2 and TiO_2

$t_{lossy} = 20$ nm. In addition, too thinner Fe film might not be continuous, leading its refractive index to deviate notably from that of bulk Fe. Hence, the thickness of the Fe film was set at 13 nm.

To elucidate the contributions of SiO_2 and TiO_2 films, we assessed the variation of the reflection spectra with their respective thicknesses. Figure 3(a)–(i) present the calculated contour map of reflection for the stacked film plotted against the thicknesses of TiO_2 and SiO_2. Regions of low reflection (depicted in deep blue) emerge periodically at wavelengths $\lambda = 350$–900 nm with increasing thicknesses of SiO_2 and TiO_2. For wavelengths ranging from $\lambda = 1000$ nm to 1100 nm, a singular region of low reflectivity was obtained in each contour map. When there was no TiO_2 film ($t_{high-n} = 0$), the vanishing condition of the reflection at $\lambda = 350$ nm to 1100 nm could not be observed for any thickness of SiO_2. This implies that a TiO_2 layer of appropriate thickness is instrumental in mitigating the stark index contrast between the Ag/SiO_2/Fe stack and air. Compared with the TiO_2 thickness dependence, we observed that low-reflection zones were more invariant to SiO_2 thickness, evident from the horizontally extended form of such regions. However, when the SiO_2 film was omitted ($t_{low-n} = 0$), reflectivity surged at extended wavelengths beyond $\lambda = 600$ nm. For instance, reflectivity below 9.17% (for $\lambda = 600$ nm to 1100 nm) was not observed at any TiO_2 thickness when SiO_2 was absent. Based on the calculated reflection

Optical Materials EXPRESS

contours, we determined the optimal parameters for the multilayer structure: $t_{low-n} = 70$ nm, $t_{lossy} = 13$ nm, and $t_{high-n} = 60$ nm.

To elucidate the absorption characteristics and spatial distribution within the designed $Ag/SiO_2/Fe/TiO_2$ multilayered structure, we performed FDTD simulations of the electromagnetic field distribution using the commercial software Fullwave by Synopsys Inc. As depicted in Fig. 1, a periodic boundary condition was applied to the x- and y- directions, assuming each film to be infinite along these axes. A perfectly matched layer, which neither reflected nor affected the field's amplitude, was set in the z-direction. The medium of incidence (air) and Ag layer were treated as infinitely thick. To assess the absorption performance and spatial distribution, spatial grids of 2 and 1 nm were utilized, respectively. The refractive indices of each layer were sourced from previously published works [43–46]. Using both TMM and FDTD methods, we calculated the reflection and absorption spectra of this design, as illustrated in Fig. 4. The solid curves and open circles in Fig. 4 represent the TMM and FDTD calculation results, respectively. The reflectivity calculated via TMM showed extremely good agreement with that obtained using the FDTD method. Given that the substantial Ag layer both dampens transmitted light and almost perfectly reflects it, we defined absorption (A) as $(100 - R)\%$. The reflectivity of the refined multilayer film is considerably suppressed for wavelengths within $\lambda = 400$–1100 nm. With both T and R diminishing, light is constrained within the stacked film. Consequently, the spectrum shows an average absorption of 94.8%, peaking at 99.9% for $\lambda = 900$ nm.

To elucidate the specific contributions of each layer toward the broadband near-perfect absorption characteristics, we introduce an optical admittance diagram for our layered assembly [47]. Figure 5 displays the complex optical admittance across various wavelengths. The optical admittance (Y) is relative to that of air (our incident medium). Reflectivity is expressed as $(1 - Y)^2/(1 + Y)$,[2] with reflection being entirely suppressed at $Y = 1 + 0i$ (corresponding to the

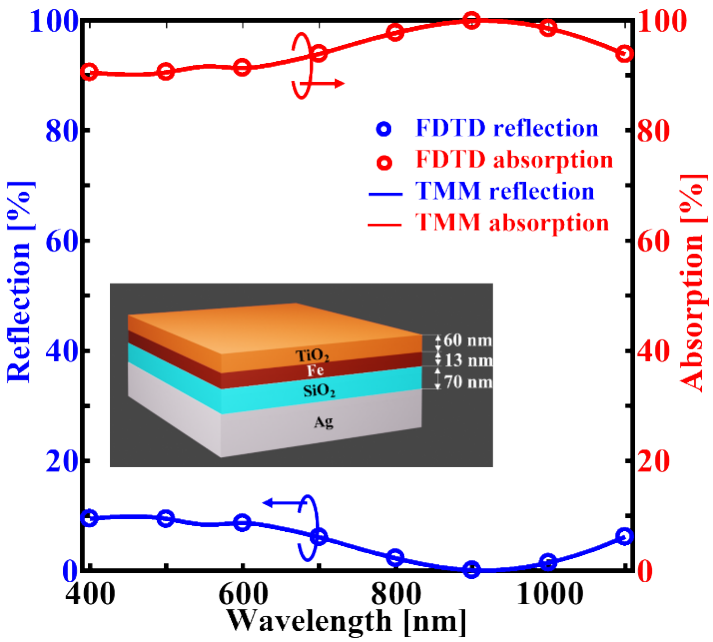

Fig. 4. Calculated reflection and absorption spectrum of the designed $Ag/SiO_2/Fe/TiO_2$ absorber. The Ag is assumed to be of infinite thickness. The thickness of SiO_2, Fe, and TiO_2 are 70, 13, and 60 nm, respectively. The solid lines and open circles indicate TMM and FDTD calculation results.

Optical Materials EXPRESS

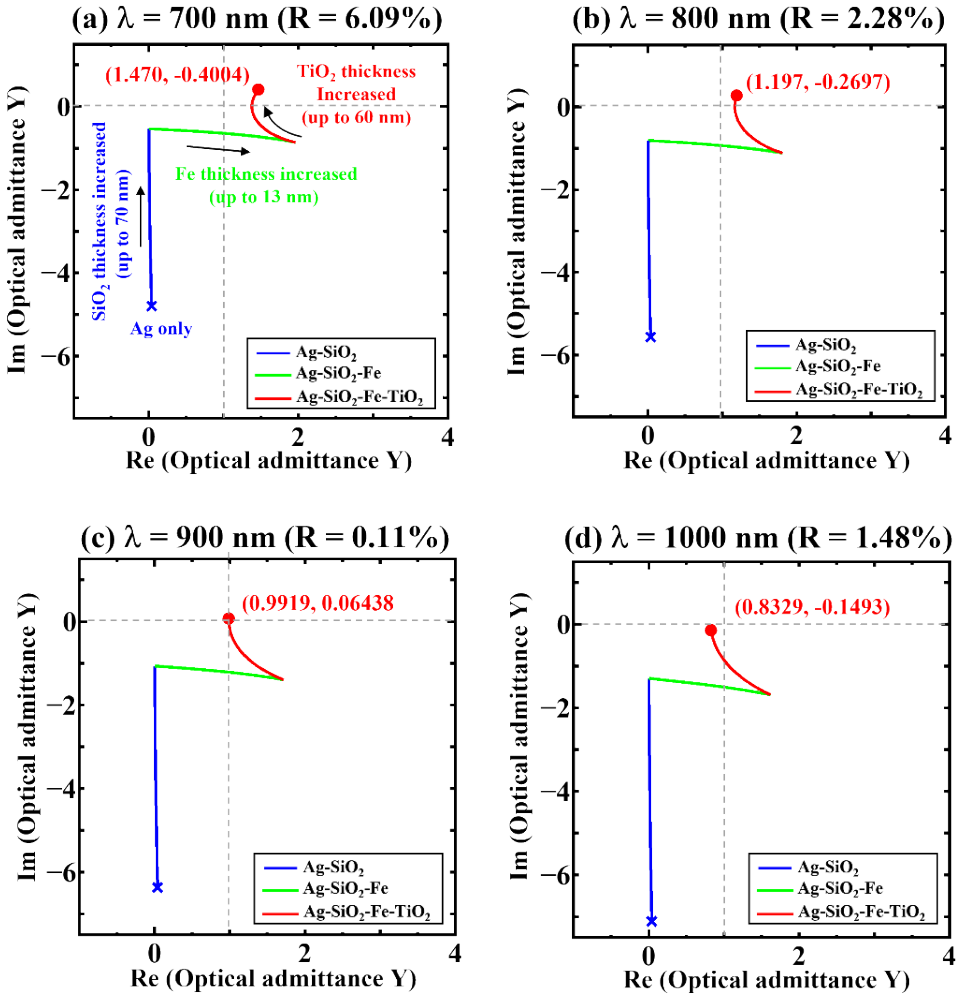

Fig. 5. Complex optical admittance diagram of our broadband absorber (a) at λ = 700 nm, (b) at λ = 800 nm, (c) at λ = 900 nm, and (d) at λ = 1000 nm. The blue crosses and red filled circles indicate the admittance of only Ag substrate and optimized Ag/SiO_2/Fe/TiO_2 stacking film, respectively. The intersection of the dashed gray lines shows the admittance of air.

air index). The admittances of the Ag substrate, denoted by the blue cross in Fig. 5, manifest as significant, complex values, and exhibit stark contrast to that of air across all wavelengths. This suggests that the Ag substrate functions as an almost perfect reflector, resulting in nearly full reflection at its surface. As SiO_2 thickness increases, the imaginary components of the admittances for all scenarios draw closer to those of air (illustrated by the blue lines in Fig. 5), highlighting the SiO_2 layer's role in moderating the contrast of the imaginary part of the admittance between Ag and air.

Increasing the thickness of the Fe film leads to a more pronounced admittance disparity with air. This stark admittance contrast is mitigated by a suitably thick TiO_2 layer. As TiO_2 thickness grows, admittance contrast diminishes, resulting in the overall admittance of the designed Ag/SiO_2/Fe/TiO_2 closely aligning with that of air across all wavelengths (the terminating red point depicts the complete admittance of the optimal structure). Thus, the diagram elucidates the

Optical Materials EXPRESS

pivotal roles played by the SiO_2 and TiO_2 layers in ensuring admittance alignment. Both layers are instrumental in achieving ultra-broadband absorption in the deeply subwavelength Fe film.

3. Experimental results and discussion

The broadband absorber, refined through optimization, was manufactured using resistive heating and electron-beam evaporation techniques. An Ag film was deposited onto a pre-cleaned optical glass. Subsequently, SiO_2, Fe, and TiO_2 films were sequentially evaporated using an electron beam. The pressure within the evaporation chamber was maintained below 4.58×10^{-4} Pa. The evaporation rates for Ag, SiO_2, Fe, and TiO_2 were set to 1.0, 1.0, 0.5, and 0.5 Å/s, respectively. Figure 6 presents a scanning electron microscopy (SEM) image of the sample's cross-section, with a scale bar marking 500 nm. The experimentally determined thicknesses for the Ag, SiO_2, Fe, and TiO_2 layers were 85 nm, 70 nm, 13 nm, and 60 nm, respectively.

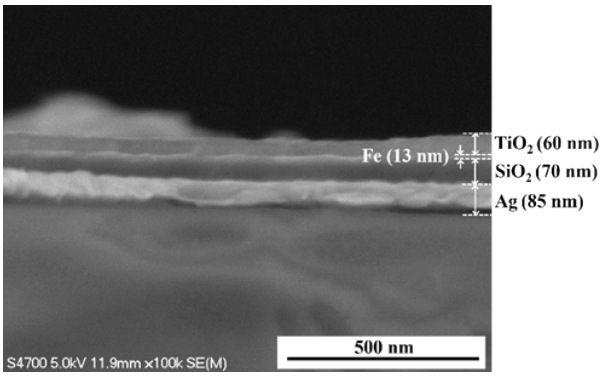

Fig. 6. SEM image of the cross-section of the evaporated Ag/SiO_2/Fe/TiO_2 film onto glass substrate. The scale bar shows 500 nm.

We measured the reflectivity and transmittance of the fabricated Ag/SiO_2/Fe/TiO_2 sample using a tunable monochromatic light source coupled with a photodetector. A reflection probe (R200-7-UV-VIS from Ocean Insight, Inc.) was employed to measure the reflection property of the fabricated samples using a tunable monochromatic light emitter (NIJI-2KK by Bunkoukeiki Co., Ltd.) as a broadband light source. The beam size of the incident light is about 200 µm. The transmitted and reflected light intensities were quantified using a photodetector and an electrometer (6517A by Keithley Co., Ltd.). For the measurement, an ultra-broadband dielectric multilayer mirror (TFMS-30C05-4/20 by Sigma Co., Ltd.) was used as the reference. The reflectivity of the sample was adjusted in accordance with that of the reference mirror.

Figure 7 displays the experimentally measured reflection and absorption spectra for the samples. The experimental data presented in Fig. 7 represent the mean values obtained from three measurements. An inset in Fig. 7 provides a photograph of the constructed sample, with the Ag/SiO_2/Fe/TiO_2 region appearing black. Within Fig. 7, filled circles and continuous lines denote the experimental results and TMM calculations, respectively. We define the measured absorption as $A = 100 - T - R$. Our experiments confirmed that T was nearly zero, as the light intensity passing through the sample was beneath the detection threshold of both the photodetector and electrometer. Hence, A was determined to be $100 - R$. Figure 7 demonstrates that our fabricated absorber effectively diminishes reflection, exhibiting an average reflectivity of 5.2% across the wavelength span of 400 to 1100 nm. As a result, an average absorption of 94.8% was experimentally validated across the VIS to NIR wavelength range. Notably, the peak absorption exceeded 99.3% at a wavelength of 850 nm, despite the deeply subwavelength-sized Fe absorptive film. The experimentally measured absorption spectrum closely aligned with our calculations.

Optical Materials EXPRESS

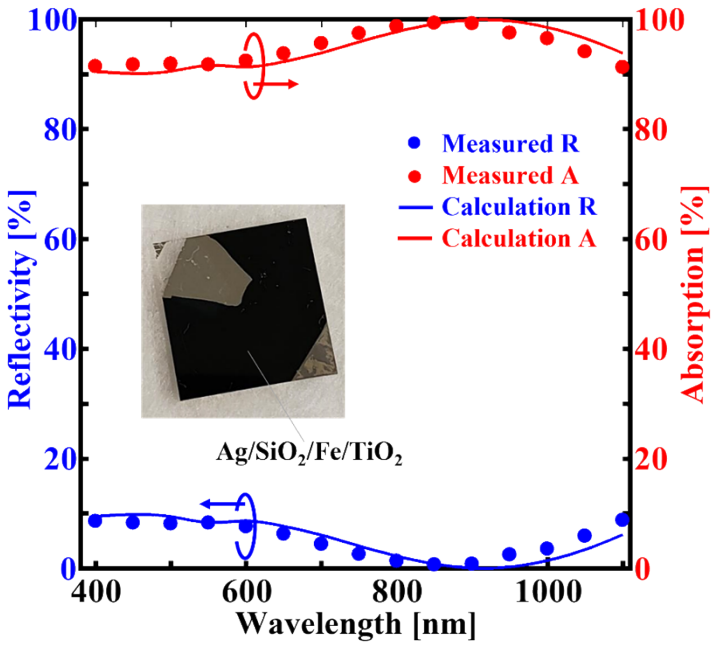

Fig. 7. Measured normal reflectivity and absorption spectra of the fabricated Ag (85 nm)/SiO_2 (70 nm)/Fe (13 nm)/TiO_2 (60 nm) structure in the wavelength region from 400 nm to 1100 nm. The inset photograph is the optical image of the fabricated sample. The data are the mean values obtained from three measurements.

The slight difference between the experimental and calculation results can be attributed to the following two imperfectness during fabrication. (i) Non-uniformity of the film thicknesses (See Fig. 6). Especially, the fluctuation of Fe film thickness mainly causes the change of the absorption characteristic because the thickness is very thin. (ii)The refractive index deviation between each evaporated film and those in the calculation. Although the measured characteristics contain the imperfectness, the good agreement between the experiment and the calculation means its influence is enough small.

To obtain a more profound understanding of the observed absorption features, we computed the spatial distribution of the electromagnetic field. The spatial absorption and Poynting vector distributions were computed using the formulas: $\omega \mathrm{Im}[\varepsilon(z)] \mid E(z) \mid^2$ and $\boldsymbol{E}(z) \times \boldsymbol{H}^*$ (z), where ω, $E(z)$, $H(z)$, and $\varepsilon(z)$ represent the incident light's angular frequency, steady-state electric field, steady-state magnetic field, and dielectric function, respectively. Figure 8(a)–(e) delineate the calculated absorption patterns across a vertical cross-section of Ag/SiO_2/Fe/TiO_2 for various wavelengths. The Ag substrate showed negligible absorption, emphasizing its role as an excellent reflector for wavelengths exceeding $\lambda = 400$ nm. Therefore, absorption predominantly transpired within the extremely thin 13-nm Fe film for these wavelength instances. At $\lambda = 400$ nm, we detected minimal absorption within the Ag substrate (Fig. 8(a)). This result suggests that light with a wavelength of 400 nm marginally penetrates the Ag substrate, given that this wavelength is proximate to the plasma wavelength of Ag (which is approximately 340 nm) [43]. Moreover, the calculated Poynting vector distributions at different wavelengths are shown in Fig. 9. The magnitude of the Poynting vectors significantly decreases in the Fe film, and the distributions indicate that the almost all the light energy dissipates into the ultrathin 13-nm Fe film. Our findings underscore the ability of our layered film assembly to achieve broadband near-perfect absorption spanning from VIS to NIR wavelengths solely within a 13-nm Fe film. Such expansive

Optical Materials EXPRESS

absorption within this ultrathin layer has considerable potential applications, including efficient light-to-heat conversion owing to the minimized heat capacity of the ultrathin film.

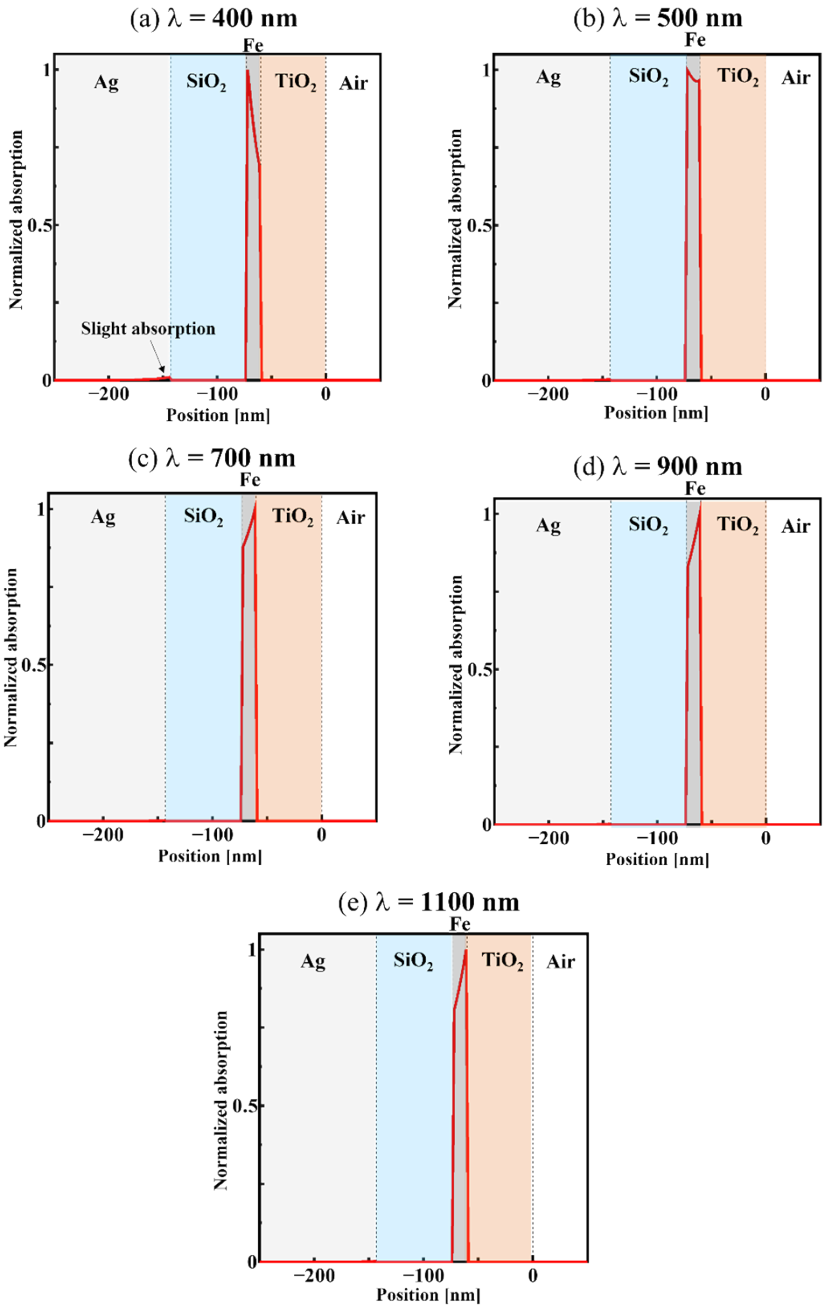

Fig. 8. Normalized spatial distribution of absorption inside the optimized $Ag/SiO_2/Fe/TiO_2$ stacking film (a) at $\lambda = 400$ nm, (b) at $\lambda = 500$ nm, (c) at $\lambda = 700$ nm, (d) at $\lambda = 900$ nm, and (e) at $\lambda = 1100$ nm.

We further investigated the angular reliance of our sample's absorption spectra, given the significance of this characteristic for the real-world application of an ideal absorber. To determine

Optical Materials EXPRESS

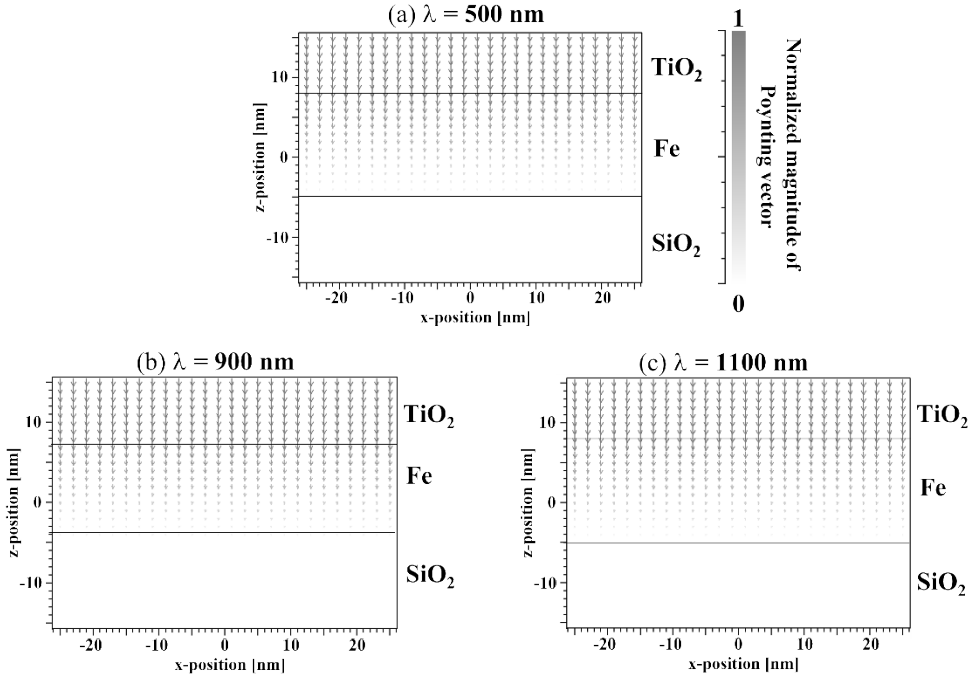

Fig. 9. Normalized Poynting vector distribution inside the optimized Ag/SiO_2/Fe/TiO_2 stacking film (a) at $\lambda = 500$ nm, (b) at $\lambda = 900$ nm, (c) at $\lambda = 1100$ nm.

the angular dependence of absorption, the incident light was polarized and collimated using a Glan–Thompson polarizer (GTPB-15-32.5SN by Sigma Co. Ltd.) and collimator (COL005S0101 from Ocean Photonics Co. Ltd.). The beam size of the light from the collimator is about 250 µm. Light was directed at the sample at an angle θ, and the intensity of the specularly reflected light was recorded using a photodetector. The angular dependence of the absorption spectra for s-, p-, and unpolarized light is depicted in Fig. 10 (Fig. 10(a), (c), and (e) show the measured values, whereas Fig. 10(b), (d), and (f) depict the calculated ones). p- and s-polarized electric fields align parallel and perpendicular to the incident plane, respectively. The experimental data presented in Fig. 10 represent the mean values obtained from three measurements. Absorption of unpolarized light is calculated as the mean of absorption for s- and p-polarizations. For s-polarization, as illustrated in Fig. 10(a), an absorption peak at 800 nm was evident. The absorption spectrum at $\theta = 30°$ closely resembled the spectrum at $\theta = 0°$. Absorption magnitudes diminished as the incident angle θ increased from 30° to 60°. However, the spectral configurations remained relatively unaffected by changes in the angle of incidence. At $\theta = 60°$, an average absorption of 80.7% from 400 to 1100 nm was observed.

In the case of p-polarization, as shown in Fig. 10(c), an absorption peak was discernible at 800 nm when $\theta = 30°$. As θ increased, the peak for p-polarization absorption exhibited a blue shift. Across wavelengths from 400 to 1100 nm, average absorption for p-polarization remained at 90.0% even at $\theta = 60°$, surpassing s-polarization. The discrepancies between s- and p-polarizations may be attributed to variances in effective optical admittances during oblique incidences. Tilted admittances of the L-th film for s- and p-polarization, denoted by Y_L, are determined by $Y_L = (n_L + k_L\mathrm{i})\cos\theta_L/\cos\theta$ and $(n_L + k_L\mathrm{i})\cos\theta\ /\cos\theta_L$, respectively [47]. Here, $n_L + k_L\mathrm{i}$ and θ_L represent the complex refractive index and propagation angle of the L-th film, respectively. Thus, the difference in admittance between the s- and p-polarizations increases with increasing values of θ. This trend results in different absorption characteristics for each

Optical Materials EXPRESS

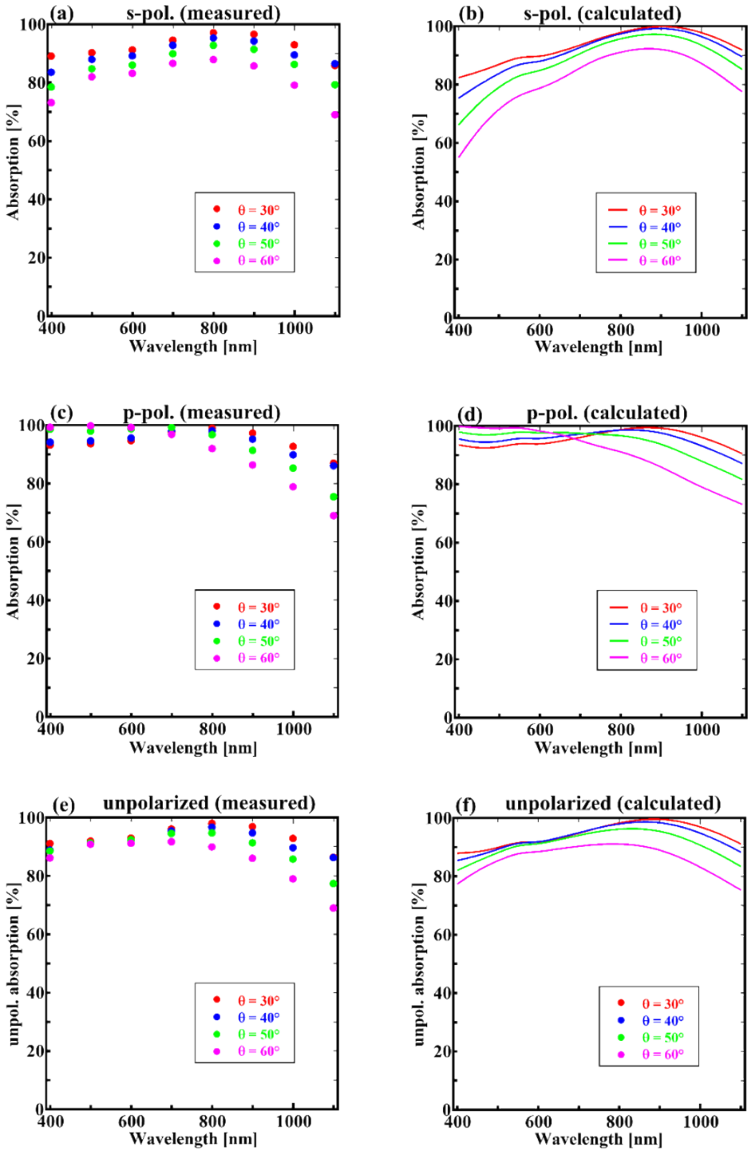

Fig. 10. Angular dependence of the absorption spectra. (a), (c), and (e) show the measured values for s-polarization, p-polarization, and unpolarized light, respectively. (b), (d), and (f) show the TMM calculated spectra for each polarization state. The data represent the mean values obtained from three measurements.

orthogonal polarization, particularly for cases in which θ is large, and provides an explanation for the angular dependence of absorption of our stacked system. Consequently, a consistent absorption of 85.4% was observed for unpolarized light with an incidence angle of $\theta = 60°$, as shown in Fig. 10(e). The measured spectra concurred closely with our computational results, as evident in Fig. 10(b), (d), and (f). The measured angular reliance of absorption traits suggests that our absorber holds promise for practical applications such as thermal emitters. Broadband and wide-angle absorption within ultrathin singular layers enhances the efficiency of light-to-thermal energy conversion.

Optical Materials EXPRESS

4. Conclusions

In this study, we designed a broadband ultrathin absorber using an $Ag/SiO_2/Fe/TiO_2$ composite. Analysis of the complex optical admittance diagram revealed that the SiO_2 and TiO_2 films substantially reduced the admittance difference between the stacked system and ambient air. This design effectively minimized both reflectivity and transmission across an extensive range of wavelengths. Simulations using the FDTD method showed that the slender Fe film, despite its minimal thickness, absorbed nearly all the incident light energy. Utilizing the vacuum evaporation technique, we manufactured the proposed absorber and achieved an average absorption of 94.8% for wavelengths between 400 to 1100 nm under standard incidence. Notably, we observed a peak absorption value of 99.3% at a wavelength of 850 nm. Further investigations into the angular dependence of the absorption spectra confirmed that our absorber sustained an 85.4% absorption rate for wavelengths from 400 to 1100 nm, even with a 60° inclined incidence of unpolarized light. Given these attributes, our absorber offers significant potential for various applications, notably in the conversion of light to thermal energy. Its low heat capacity, broad spectral compatibility, wide-angle adaptability, and cost-effective, scalable fabrication process that bypasses the need for lithography, position it as a valuable tool. Our findings underscore the potential applicability of Fe as an optical absorber. In subsequent studies, we plan to develop a high-efficiency thermal emitter using our groundbreaking ultrathin broadband absorber.

Funding. Japan Society for the Promotion of Science (JP21K14515).

Acknowledgments. We thank C. Azuma and S. Sugano of Tokushima University for their technical support with SEM measurements.

Disclosures. The authors declare no conflicts of interest.

Data availability. Data underlying the results presented in this paper are not publicly available at this time but may be obtained from the authors upon reasonable request.

References

1. H. S. Kim, I. Mora-Sero, V. Gonzalez-Pedro, *et al.*, "Mechanism of carrier accumulation in perovskite thin-absorber solar cells," Nat. Commun. **4**(1), 2242 (2013).
2. H. Meddeb, M. Götz-Köhler, N. Neugebohrn, *et al.*, "Tunable photovoltaics: adapting solar cell technologies to versatile applications," Adv. Energy Mater. **12**(28), 2200713 (2022).
3. Z. Xia, H. Song, M. Kim, *et al.*, "Single-crystalline germanium nanomembrane photodetectors on foreign nanocavities," Sci. Adv. **3**(7), e1602783 (2017).
4. A. Ghobadi, Y. Demirag, H. Hajian, *et al.*, "Spectrally selective ultrathin photodetectors using strong interference in nanocavity design," IEEE Electron Device Lett. **40**(6), 925–928 (2019).
5. A. Lenert, D. M. Bierman, Y. Nam, *et al.*, "A nanophotonic solar thermophotovoltaic device," Nat. Nanotechnol. **9**(2), 126–130 (2014).
6. J. K. Tong, W. C. Hsu, Y. Huang, *et al.*, "Thin-film 'thermal well'emitters and absorbers for high-efficiency thermophotovoltaics," Sci. Rep. **5**(1), 10661 (2015).
7. M. Diem, T. Koschny, and C. M. Soukoulis, "Wide-angle perfect absorber/thermal emitter in the terahertz regime," Phys. Rev. B **79**(3), 033101 (2009).
8. G. Liu, X. Liu, J. Chen, *et al.*, "Near-unity, full-spectrum, nanoscale solar absorbers and near-perfect blackbody emitters," Sol. Energy Mater. Sol. Cells **190**, 20–29 (2019).
9. N. I. Landy, S. Sajuyigbe, J. J. Mock, *et al.*, "Perfect metamaterial absorber," Phys. Rev. Lett. **100**(20), 207402 (2008).
10. J. Hao, J. Wang, X. Liu, *et al.*, "High performance optical absorber based on a plasmonic metamaterial," Appl. Phys. Lett. **97**(18), 251104 (2010).
11. S. Gu, J. P. Barrett, T. H. Hand, *et al.*, "A broadband low-reflection metamaterial absorber," J. Appl. Phys. **108**(6), 064913 (2010).
12. F. Ding, Y. Cui, X. Ge, *et al.*, "Ultra-broadband microwave metamaterial absorber," Appl. Phys. Lett. **100**(10), 103506 (2012).
13. R. Yahiaoui, K. Hanai, K. Takano, *et al.*, "Trapping waves with terahertz metamaterial absorber based on isotropic Mie resonators," Opt. Lett. **40**(13), 3197–3200 (2015).
14. D. Hasan, P. Pitchappa, J. Wang, *et al.*, "Novel CMOS-compatible Mo–AlN–Mo platform for metamaterial-based mid-IR absorber," ACS Photonics **4**(2), 302–315 (2017).
15. F. Kiani, F. Sterl, T. V. Tsoulos, *et al.*, "Ultra-broadband and omnidirectional perfect absorber based on copper nanowire/carbon nanotube hierarchical structure," ACS Photonics **7**(2), 366–374 (2020).

Optical Materials EXPRESS

16. Y. Huang, K. Kaj, C. Chen, *et al.*, "Broadband terahertz silicon membrane metasurface absorber," ACS Photonics **9**(4), 1150–1156 (2022).
17. S. Huang, Z. Xie, W. Chen, *et al.*, "Metasurface with multi-sized structure for multi-band coherent perfect absorption," Opt. Express **26**(6), 7066–7078 (2018).
18. Y. Huang, L. Liu, M. Pu, *et al.*, "A refractory metamaterial absorber for ultra-broadband, omnidirectional and polarization-independent absorption in the UV-NIR spectrum," Nanoscale **10**(17), 8298–8303 (2018).
19. X. Liu, Z. Zhang, C. Han, *et al.*, "Broadband long-wave infrared high-absorption of active materials through hybrid plasmonic resonance modes," Discov. Nano. **18**(1), 35 (2023).
20. Y. Pan, Y. Li, F. Chen, *et al.*, "An ultra-broadband solar absorber based on α-GST/Fe metamaterials from visible light to mid-infrared," Phys. Chem. Chem. Phys. **25**(40), 27586–27594 (2023).
21. W. Dallenbach and W. Kleinsteuber, "Reflection and absorption of decimeter-waves by plane dielectric layers," Hochfreq. u Elektroak **51**, 152–156 (1938).
22. R. L. Fante and M. T. McCormack, "Reflection properties of the Salisbury screen," IEEE Trans. Antennas Propag. **36**(10), 1443–1454 (1988).
23. C. S. Park, V. R. Shrestha, S. S. Lee, *et al.*, "Omnidirectional color filters capitalizing on a nano-resonator of Ag-TiO_2-Ag integrated with a phase compensating dielectric overlay," Sci. Rep. **5**(1), 8467 (2015).
24. A. T. Doan, T. D. Dao, S. Ishii, *et al.*, "Gires-Tournois resonators as ultra-narrowband perfect absorbers for infrared spectroscopic devices," Opt. Express **27**(12), A725–A737 (2019).
25. C. S. Park and S. S. Lee, "Narrowband and flexible perfect absorber based on a thin-film nano-resonator incorporating a dielectric overlay," Sci. Rep. **10**(1), 17727 (2020).
26. M. A. Kats, R. Blanchard, P. Genevet, *et al.*, "Nanometer optical coatings based on strong interference effects in highly absorbing media," Nat. Mater. **12**(1), 20–24 (2013).
27. J. Park, J. H. Kang, A. P. Vasudev, *et al.*, "Omnidirectional near-unity absorption in an ultrathin planar semiconductor layer on a metal substrate," ACS Photonics **1**(9), 812–821 (2014).
28. J. Park, S. J. Kim, and M. L. Brongersma, "Condition for unity absorption in an ultrathin and highly lossy film in a Gires–Tournois interferometer configuration," Opt. Lett. **40**(9), 1960–1963 (2015).
29. Z. Li, E. Palacios, S. Butun, *et al.*, "Omnidirectional, broadband light absorption using large-area, ultrathin lossy metallic film coatings," Sci. Rep. **5**(1), 15137 (2015).
30. C. Yang, C. Ji, W. Shen, *et al.*, "Compact multilayer film structures for ultrabroadband, omnidirectional, and efficient absorption," ACS Photonics **3**(4), 590–596 (2016).
31. M. A. Kats and F. Capasso, "Optical absorbers based on strong interference in ultra-thin films," Laser Photonics Rev. **10**(5), 735–749 (2016).
32. Z. Yang, Y. Zhou, Y. Chen, *et al.*, "Reflective color filters and monolithic color printing based on asymmetric Fabry–Perot cavities using nickel as a broadband absorber," Adv. Opt. Mater. **4**(8), 1196–1202 (2016).
33. S. Abedini Dereshgi, A. Ghobadi, H. Hajian, *et al.*, "Ultra-broadband, lithography-free, and large-scale compatible perfect absorbers: The optimum choice of metal layers in metal-insulator multilayer stacks," Sci. Rep. **7**(1), 14872 (2017).
34. M. Aalizadeh, A. Khavasi, B. Butun, *et al.*, "Large-area, cost-effective, ultra-broadband perfect absorber utilizing manganese in metal-insulator-metal structure," Sci. Rep. **8**(1), 9162 (2018).
35. J. Zhang, R. Wei, M. ElKabbash, *et al.*, "Thin-film perfect infrared absorbers over single-and dual-band atmospheric windows," Opt. Lett. **45**(10), 2800–2803 (2020).
36. K. V. Sreekanth, R. Medwal, Y. K. Srivastava, *et al.*, "Dynamic color generation with electrically tunable thin film optical coatings," Nano Lett. **21**(23), 10070–10075 (2021).
37. Y. Takashima, K. Nagamatsu, M. Haraguchi, *et al.*, "Ultra-thin deep ultraviolet perfect absorber using an Al/TiO_2/AlN system," Opt. Express **30**(24), 44229–44239 (2022).
38. H. Cai, M. Wang, Z. Wu, *et al.*, "Design of multilayer planar film structures for near-perfect absorption in the visible to near-infrared," Opt. Express **30**(20), 35219–35231 (2022).
39. M. Kats, D. Sharma, J. Lin, *et al.*, "Ultra-thin perfect absorber employing a tunable phase change material," Appl. Phys. Lett. **101**(22), 221101 (2012).
40. Y. Guo, Y. Zhang, X. Chai, *et al.*, "Tunable broadband, wide angle and lithography-free absorber in the near-infrared using an ultrathin VO_2 film," Appl. Phys. Express **12**(7), 071005 (2019).
41. E. Hu, T. Gu, S. Guo, *et al.*, "Tunable broadband near-infrared absorber based on ultrathin phase-change material," Opt. Commun. **403**, 166–169 (2017).
42. K. Sreekanth, S. Han, and R. Singh, "$Ge_2Sb_2Te_5$-based tunable perfect absorber cavity with phase singularity at visible frequencies," 30(21), 1706696 (2018).
43. P. B. Johnson and R. W. Christy, "Optical constants of the noble metals," Phys. Rev. B **6**(12), 4370–4379 (1972).
44. P. B. Johnson and R. W. Christy, "Optical constants of transition metals: Ti, V, Cr, Mn, Fe, Co, Ni, and Pd," Phys. Rev. B **9**(12), 5056–5070 (1974).
45. S. Sarkar, V. Gupta, M. Kumar, *et al.*, "Hybridized guided-mode resonances via colloidal plasmonic self-assembled grating," ACS Appl. Mater. Interfaces **11**(14), 13752–13760 (2019).
46. L. Gao, F. Lemarchand, and M. Lequime, "Refractive index determination of SiO2 layer in the UV/Vis/NIR range: Spectrophotometric reverse engineering on single and bi-layer designs," J. Eur. Opt. Soc. **8**, 13010 (2013).
47. H. A. Macleod, *Thin-Film Optics*, 4th ed. (CRC Press, 2010).